

---

15 Feb 2022

## Control of High-Temperature Static and Transient Thermomechanical Behavior of SiMo Ductile Iron by Al Alloying

Semen Naumovich Lekakh

*Missouri University of Science and Technology*, lekakhs@mst.edu


Catherine E. Johnson

*Missouri University of Science and Technology*, johnsonce@mst.edu

L. Godlewski

Mei Li

Follow this and additional works at: [https://scholarsmine.mst.edu/matsci\\_eng\\_facwork](https://scholarsmine.mst.edu/matsci_eng_facwork)

 Part of the [Metallurgy Commons](#), and the [Mining Engineering Commons](#)

---

### Recommended Citation

S. N. Lekakh et al., "Control of High-Temperature Static and Transient Thermomechanical Behavior of SiMo Ductile Iron by Al Alloying," *International Journal of Metalcasting*, Springer, Feb 2022.

The definitive version is available at <https://doi.org/10.1007/s40962-022-00768-y>



This work is licensed under a [Creative Commons Attribution 4.0 License](#).

This Article - Journal is brought to you for free and open access by Scholars' Mine. It has been accepted for inclusion in Materials Science and Engineering Faculty Research & Creative Works by an authorized administrator of Scholars' Mine. This work is protected by U. S. Copyright Law. Unauthorized use including reproduction for redistribution requires the permission of the copyright holder. For more information, please contact [scholarsmine@mst.edu](mailto:scholarsmine@mst.edu).

# CONTROL OF HIGH-TEMPERATURE STATIC AND TRANSIENT THERMOMECHANICAL BEHAVIOR OF SiMo DUCTILE IRON BY Al ALLOYING

S. N. Lekakh  and C. Johnson

Missouri University of Science and Technology, Rolla, MO 65409, USA

L. Godlewski and Mei Li

Ford Motor Company, Dearborn, MI 48124, USA

Copyright © 2022 The Author(s)  
<https://doi.org/10.1007/s40962-022-00768-y>

## Abstract

Silicon and molybdenum (SiMo) ductile iron is commonly used for exhaust manifolds because these components experience thermal cycling in oxidizing environment, which requires resistance to fatigue during transient thermomechanical loads. Previous studies have demonstrated that alloying elements, such as Al, to SiMo ductile iron reduces the amount of surface degradation during static high-temperature exposure. However, deterioration of sphericity of the graphite nodules and a decrease in ductility could affect the tendency of cracking during thermal cycling. In this article, the effect of Al alloying on static and transient thermomechanical behavior of SiMo ductile iron was investigated to optimize the amount of Al alloying. A thermodynamic approach was used to confirm the effect of the Al alloying on the phase transformations in two SiMo cast irons, alloyed by 1.8% Al and 3% Al. These two alloys were cast in a laboratory along with the baseline SiMo ductile iron. Several experimental methods were used to evaluate the dimensional stability, physical

properties, static oxidation, and failure resistance during constrained thermal cycling testing to compare their high-temperature capability. Experimental results verified that Al alloying increases the temperature range and decreases volume change during eutectoid transformation, which together with enhancement of oxidation protection improved the dimensional stability. Thermocycling tests showed that the number of cycles to failure depends on the amount of Al alloying and the applied high-temperature exposure during each cycle. SEM/EDX, high-resolution TEM and  $\mu$ CT analysis were used to verify the mechanism resulting from the Al alloying protection. It was shown that an optimal level of Al alloying for balancing oxidation and thermal cracking resistance depends on thermomechanical conditions of application.

**Keywords:** ductile iron, aluminum alloying, thermomechanical behavior

## Introduction

Ferritic SiMo ductile cast iron contains 3.5–5.1% silicon and 0.4–1.1% molybdenum (wt.%), which is commonly used for high-temperature applications primarily because of its good thermomechanical properties, resistance to high-temperature oxidation, and castability.<sup>1–3</sup> One version of this alloy, designated as SiMo51 ductile iron, contains near 3.1% C, 4.1% Si, 0.4% Mn, 0.8% Mo, and 0.05% Mg and is commonly used in the manufacture of exhaust manifolds.<sup>1–5</sup> In addition to being exposed to harsh high-

temperature oxidizing environments, manifolds are subjected to the thermomechanical loadings during thermal cycling at mechanically constrained conditions. When these types of situations occur, there is a self-generated stress and strain condition, which is a function of both intrinsic (thermal expansion, heat conductivity and mechanical properties of material) and extrinsic (thermal load, component geometry) conditions. Therefore, it is important to understand the high-temperature physical-mechanical properties of a material. Combustion engine temperatures are continually being increased and operational temperatures of exhaust gas can reach as high as 1000 °C, which significantly surpasses the current temperature limit (<800 °C) for SiMo ductile iron.<sup>6</sup> Therefore,

the possibilities of extending the usage temperature of the *SiMo*51 ductile iron were investigated by applying different approaches. These approaches included optimization of *Si* and *Mo* concentrations,<sup>7</sup> small altering micro-alloying additions,<sup>8</sup> macro-alloying<sup>9-11</sup> as well as surface modification of cast component.<sup>12</sup>

It is well known that increasing the *Si* level can increase the temperature at which ferrite transforms to austenite. Therefore, raising the maximum temperature for ferritic *SiMo* cast irons can potentially reduce stress, which is caused by the volume change during the eutectoid transformation. Increasing the *Si* content improves the oxidation resistance of *SiMo* cast iron through the formation of a silicon-rich oxide surface layer, preventing the oxidation of the ferritic matrix at elevated temperatures in air.<sup>9</sup> There are some data that indicates that *SiMo* cast iron exhibits less resistance to oxidation in atmospheres containing water vapor above 650 °C.<sup>13</sup> *Si* levels up to 4 wt.% are known to improve mechanical properties and machinability of ferritic ductile cast irons.<sup>13</sup> It is well known that *Si* levels above 4.0% can lead to a dramatic decrease in certain mechanical properties at low temperatures. Warm temperature brittleness can also become a major concern when *Si* levels are in the range of 4.5–5.0%.

Molybdenum when added to *SiMo* ductile iron is known to increase the high-temperature tensile strength and resistance to creep rupture due to the formation of a network of complex *Fe-Mo* carbides, which reside at the grain boundaries. The high-temperature behavior of two types of heat-resistant *SiMo* ductile cast iron with 0.4% *Mo* and 1.0% *Mo* was examined.<sup>7</sup> The higher *Mo*-alloyed ductile iron was stronger but less ductile at 600 °C; however, similar properties were observed for both alloys at 800 °C, primarily due to softening and oxidation effects. The study<sup>12</sup> looked at chemical surface modification (nitriding or aluminizing) to prevent surface degradation of ductile iron during thermocycling.

Opportunities in the improvement of the oxidation resistance and thermomechanical properties of *SiMo* ductile irons by macro-alloying *Al*, *Ni* and *Cr* were discussed.<sup>9-11,15</sup> The studies indicate that *Al* is the most essential alloying element in improving the degree of static oxidation resistance of various *Fe*-based alloys while being tested at elevated temperatures.<sup>14</sup> The *Al* alloying concentrations ranging from 5% to 6% were evaluated.<sup>15,16</sup> The *SiMo*1000 with 3% *Al* and 1% *Ni* was suggested for car manifold applications.<sup>1,17</sup> Several advantages for the addition of *Al* on high-temperature properties of *SiMo* ductile iron include: (i) raising the ferrite-to-austenite phase transformation temperature, which increased the limit of operation conditions,<sup>16</sup> (ii) decreasing the negative *Si* segregation around graphite nodules,<sup>18</sup> and (iii) increasing the oxidation resistance by forming alumina surface protection barrier.<sup>9,11</sup>

In the study,<sup>19</sup> silicon segregation in a high silicon-alloyed ductile iron was specifically altered by small additions of aluminum. The results show that the fatigue strength at room temperature was increased as compared to the reference alloy containing no aluminum. At the same time, several negative effects of aluminum were reported, including sudden decrease castability and degeneration of spherical graphite shape at *Al* contents above 0.2 wt%.<sup>19</sup> When *Al* is added in larger concentrations, the study<sup>20</sup> has shown that there is significant degeneration of the graphite nodule shape, which dramatically decreases the ductility at room temperature. However, the small *Al* concentrations (<1%) are not enough to improve the high-temperature oxidation protection. While the mechanism of graphite shape degradation under influences of *Al* alloying is still unfamiliar, optimization of alloy composition and melt treatment technology for static and transient thermomechanical oxidation conditions were needed to be investigated.

Finite-element simulations (FEM) of the exhaust manifold indicate that the areas closest to exhaust gas entry become hotter as compared to other areas of the component.<sup>21</sup> This condition initiates a non-uniform thermal expansion and stress triaxiality locally throughout the component wall. Material transient thermomechanical behavior is important for exhaust manifolds. In addition to static oxidation and quasi-static high-temperature creep, they are subjected to transient heating and cooling cycles, which induce thermomechanical fatigue (TMF). When a manifold is fastened to an assembly and subjected to cyclic heating/cooling while being in a mechanically constrained, the component will experience thermal and mechanical multiaxial loading.<sup>22</sup> There is minimal information on the effects of *Al* alloying on transient thermomechanical behavior of *SiMo* ductile iron.

*This work investigates balancing the amount of Al additions to a baseline SiMo ductile iron while monitoring the high-temperature thermomechanical behavior. The article structure included thermodynamic simulations of Al-alloyed SiMo ductile iron followed by experimental study of static and transient thermomechanical behavior, pursuing the goal to optimize alloy composition for specific conditions of thermomechanical loading in oxidized atmosphere.*

## Simulation and Experimental Procedures

### Alloy Simulation and Design

**Microstructure** The additions of *Si* and *Al* in cast iron have mutual effects on the solidification and eutectoid transformation. To predict these effects, thermodynamic simulations were performed using THERMOCALC software.<sup>23</sup> It is well known that *Si* segregates and concentrates in an austenite shell formed around graphite nodules during

graphite/austenite eutectic solidification. Such segregation promotes embrittlement of the ferrite and crack initiation at graphite boundary during thermal cycling.<sup>24,25</sup> The thermodynamic simulation of ductile iron with 3% C and 4.5% Si (shown by solid black line in Figure 1) suggests that initially formed austenite around graphite nodules (low FCC fraction in Figure 1) had elevated Si levels when compared to the last fraction of solidified austenite at eutectic cell boundary. The calculated degree of the Si segregation depends on assumptions used in the applied thermodynamic models. In this study, applied equilibrium model assumed full diffusion, while the other possible models restrict back diffusion and can predict a larger negative Si segregation. The real Si segregation will be between these extremal predictions and depends on cooling rate and graphite nodule number.<sup>26</sup> So, thermodynamic prediction well-fitted experimentally observed negative Si segregation.

It has been shown that Al alloying has the possibility to significantly change the Si segregation pattern.<sup>18,27</sup> Therefore, two levels of Al alloying (1.8% and 3%) were investigated in ductile irons with adjusted Si concentrations (3.0% and 3.5, respectively) to achieve a similar near-eutectic compositions. When adding 1.8% Al, this imposed a practically flat Si distribution in austenite (black dashed line in Figure 1). High 3% Al forced switching a negative into a positive Si segregation, and the Si concentration increased in the last solidified interdendritic region (shown by black dotted line in Figure 1). These data show that Si segregation in ductile iron can be effectively controlled by Al alloying, and the simulation results agree with published data.<sup>18</sup> On the contrary to Si, Al always concentrates in the first solidified austenite shell around graphite nodules (red lines in Figure 1). This Al saturation of austenite/graphite boundary could have a positive effect on protecting decarburization (deC) of graphite nodules during high-temperature exposures and will be investigated in this work.

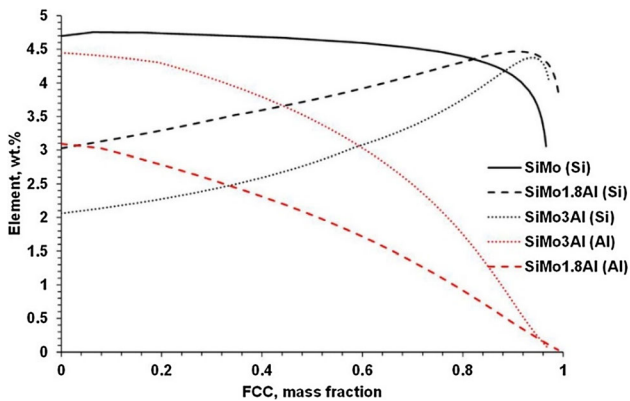


**Figure 1. Calculated (THERMOCALC) Si and Al segregations during eutectic solidification in base and Al-alloyed SiMo ductile irons**

*Density.* The addition of Si and Al increases the temperature of eutectoid reaction. Simulations showed that Al alloying provided different changes in ferrite (*Fe-BCC*) and austenite (*Fe-FCC*) lattice parameters, which resulted in decreases in total volume change during the eutectoid reaction.<sup>28</sup> These two factors are important for decreasing local stresses, which could be developed during thermal cycling of a manifold near-eutectoid reaction temperatures. As shown in Figure 2, there is a significant density increase (specific volume decrease and linear contraction) resulted by ferrite/austenite transformation during heating of the baseline SiMo ductile iron. Our simulations also showed that alloying with Al can decrease the change in density between austenite and ferrite and near-zero density change takes place during eutectoid reaction in ductile iron alloyed by 3% Al (Figure 2, dotted line).

*Oxidation.* Thermodynamic simulations of oxidation were performed with assumptions that the local equilibrium condition could be reached between the gas components, formed oxide phases, and SiMo cast iron at different distances from surface.<sup>8</sup> This method was used to predict the phases that could be formed at low (inner scale layer) and high (outer scale layer) oxygen levels. Therefore, the local equilibrium conditions were simulated (FactSage 7.3 software with FSsteel, FToxid, and FactSPS databases<sup>29</sup>) by adding oxygen stepwise into the alloy streams from the previous simulation step assuming an irreversible reaction. The results predicted the formation of multi-layered scale and deC sublayer structures in the Al-alloyed SiMo ductile iron during thermal exposure at 800°C. These results are illustrated in Figure 3, where de-C layer was formed in the matrix (black columns), followed by a protective pure alumina film at the matrix/scale interface. The complex internal and external oxidation layers are present in the scale structure. The simulation results will be compared to the experimental data.

The described thermodynamic simulations predicted several possible positive outcomes from SiMo with Al

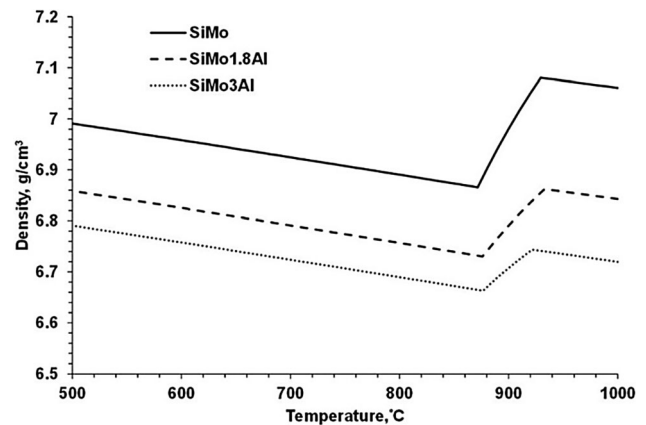


**Figure 2. Calculated (ThermoCalc) density change in base and Al-alloyed SiMo ductile irons**

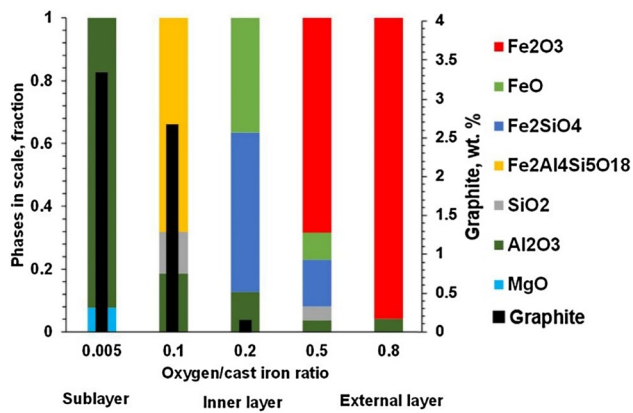


**Figure 3. Predicted (FactSage software) multi-layered structure of scale in SiMo ductile iron alloyed by 3% Al at 800 °C**

additions including a potential for controlling *Si* and *Al* segregation, an increase in the temperature transformation and a decrease in the volume change during the eutectoid reaction, as well as the formation of an alumina film at metal/scale boundary during high-temperature oxidation.

### Experimental Alloys and Test Methods

**Alloys.** Three *SiMo* ductile cast iron alloys were evaluated, including a baseline *SiMo* and two alloyed with 1.8% *Al* (*SiMo1.8Al*) and 3% *Al* (*SiMo3Al*). The alloys contained 0.7–0.8% *Mo* and 0.03–0.06% *Mg*. The *Si* and *C* concentrations in the *Al*-alloyed ductile irons were adjusted to achieve a similar near-eutectic composition for all the alloys. An additional 0.9% *Ni* was added for *Al*-alloyed ductile irons.<sup>17</sup> These alloys were melted in 200 lb. induction furnace (20% pig iron, 30% high-purity induction iron, and 50% ductile iron foundry return) and poured into no-bake silica sand molds producing 18–20-mm wall thickness keel blocks with top risers. To suppress the negative effect of *Al* on graphite shape and bi-film defects, a special proprietary melt treatment was developed, and micro-additions were applied. The specimens for structural analysis and tests were taken from the central part of keel blocks at least 1" apart from top and bottom.

**Linear expansion and eutectoid transformation temperature.** Dilatometer (DIL 402, Netzsch) tests were performed in *Ar* protection atmosphere using the following sequential thermal cycles: heating from 20 °C to 930 °C at 5 °C/min, hold for 20 min and cooled to 500 °C at 5°C/min followed by a 20-min. hold. This sequence was repeated twice to verify the dimensional stability during thermal cycling in the unconstrained condition. In addition, differential scanning calorimetry (DSC-TGA, Netzsch) was used to determine the critical transformation temperatures during heating at 10 °C/min in *SiMo3Al* ductile iron because this

alloy did not show detectable linear changes during phase transformation.

**Thermal properties.** Thermal diffusivity is an important physical property for materials used at transient temperature cycling condition; therefore, the laser flash (LF) method was used to quantify thermal diffusivity.<sup>30</sup> The LF technique requires a 12.7-mm disc of 2-mm thickness, which is subjected to a high-intensity short duration of radiant laser pulses. The energy of the pulse is absorbed on the front surface of the specimen, and the rear face temperature rise is recorded. The thermal diffusivity value (*a*) was calculated from specimen thickness (*L*) and time (*t*<sub>1/2</sub>) required for rear face temperature to reach 50% of its maximal value. To obtain reliable data, all alloys were tested simultaneously, and test was repeated twice using new samples.

**Quasi-static mechanical properties.** CNC precise machined 6-mm-diameter specimens with threaded ends were used for high-temperature tensile tests in the MTS frame equipped by the furnace with temperature controller. Displacement and tensile force were reported during a test.

**Static Oxidation.** The oxidation tests were performed on 35x14x5 mm specimens cut from the bottom part of cast keel blocks to avoid casting defects (porosity and bi-films). Each specimen was finished using wet machine grinding with 60-grit silicon carbide on all sides. The oxidation tests were conducted in air without interruption for a duration of 100 hours at 700 °C, 750 °C, and 800 °C. Oxidation was done by placing a sample into a rectangular-shaped alumina crucible to retain any loose scale particles. A two-zone horizontal quartz tube furnace, at ambient pressure, was used for these tests with +/- 1 °C temperature control. A special procedure,<sup>8</sup> for decoupling oxidation and deC by measuring weight gain and changes in *C*, wt.% were conducted. Specimens and crucibles were weighed before and after experiments to determine a total weight change ( $\Delta G$ ). A central part of a specimen was sectioned using a precision water-cooled saw to extract a thin approximately 1g sample for Leco combustion carbon analysis. This sample contained the deC perimeter, which was prior exposed to an oxidizing atmosphere during the test. A change in carbon concentration before and after the test was used to calculate a weight loss due to decarburization ( $\Delta G_C$ , g/m<sup>2</sup>). Two oxidation parameters were calculated: (i) the weight of oxygen reacted with metallic components in alloy to form scale ( $\Delta G_M$ , g/m<sup>2</sup>), which was taken from the measured weight gain ( $\Delta G$ ) and considering weight loss due to deC, and (ii) the amount of oxygen spent on deC, equals  $-1.33\Delta G_C$ , where 1.33 is a ratio of atomic mass of *O* and *C* involved in *CO* gas forming reaction)

**Thermocycling test.** To experimentally replicate an alloy behavior during thermal cycling of mechanically constrained complicated shape manifold, the thermocycling

tests were performed using a device referred to the “Thermal Simulator”. The test procedure used in this study is described in<sup>31</sup>. A special shape specimen (insert in Figure 4) was designed to test the thermal cycling behavior of the components with the local mechanical constraints. During the test, the stress triaxiality was developed by thermal expansion and contraction during thermal cycling. This test was simulated using FEM, and it identified a high probability of a crack at the internal corner area.<sup>31</sup> The temperature is computer-controlled by passing high ampere DC current through the specimen. The temperature of the specimen was monitored by an infrared pyrometer with a 1-mm spot size. The thermal simulator had compression/tension load cell from left side and electric servo-cylinder from right side. Holding grips were water-cooled. To study the effect of oxidation on crack formation during thermal cycling, three temperature/time schedules, named as “short”, “medium” and “long”, were used with variations in holding time at the maximum test temperature. All these schedules used the same minimum (300 °C) and maximum (800 °C) temperatures (Figure 4). The Thermal Simulator was set to a zero force prior to starting each test condition (300 °C) to compensate linear expansion when heating from room temperature. Once the test was started, the developed tensile force at the end of each cycle was used to monitor crack initiation, and 90% force from an original maximal force was used as threshold to report number of cycles for crack propagation.

**Structure analysis.** Samples for optical, SEM, and TEM analyses were prepared from the as-cast, oxidized, and thermocycled specimens using precision wet cut, mounting and finished with a multistep polishing technique. Deep etching with an electrolytic method was used to observe graphite phase structure.<sup>32</sup> An additional oxidation tests were performed at 800 °C for 100 hours for non-destructive test of formed scale. The formed scale on 2.9-mm-diameter specimens were subjected to a micro-computed X-ray tomography ( $\mu$ CT) with high-resolution ZEISS

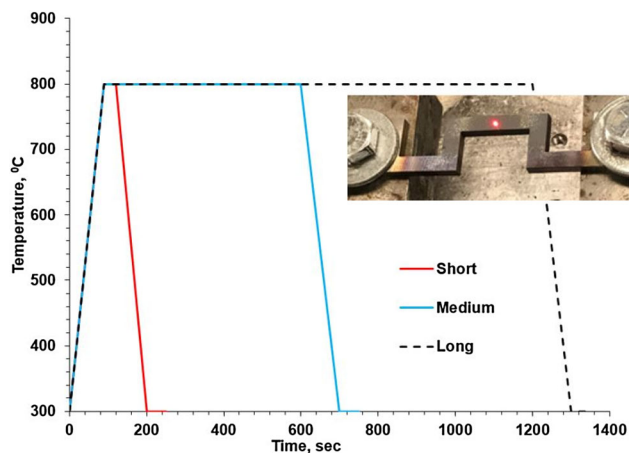


**Figure 4. Temperature–time cycle schedules and tested specimen (insert)**

Xradia 510 Versa.<sup>33</sup> To characterize the scale topology, a total of 1601 projections were taken from each specimen at 360 degrees of rotation using a 0.4X objective with a 3.5 $\mu$ m pixel size. Additional scans with 1.0  $\mu$ m pixel size were performed for graphite morphology in a central region of each specimen. Scanning electron microscopy (SEM) with energy-dispersive X-ray analysis (EDX) was performed with the ASPEX system along with backscattered electron and Omega Max EDX detectors. A TEM study was performed in the base *SiMo* and in the *SiMo1.8Al* ductile irons after fast thermal cycling. TEM samples were taken next to a crack tip in a dual-beam SEM/focused ion beam (SEM/FIB, Helios NanoLab 600, Thermo Fisher Scientific). The FIB was operated at 30 kV acceleration voltage with various emission currents ranging from 21 nA to 0.1 nA. The acceleration voltage of 200 kV TEM (Tecnai F20, Thermo Fisher Scientific) was utilized to study the detailed structure near the crack, and an EDX mapping was conducted using an Oxford X-Stream lithium drifted silicon detector. TEM-selected area diffraction pattern (SADP) was employed to study the crystallographic structure of the compounds.

## Results

**As-cast structure.** All alloys contained a ferritic matrix with *Mo* carbides located at the eutectic grain boundaries (Figure 5a–c). Graphite nodules in the base *SiMo* ductile irons had some distortions visible at higher magnification (inserts), which could be related high *Si* concentration. The  $\mu$ CT analysis was used for true 3D characterization of graphite phase (Figure 5e–g) and statistical analysis using methodology described in.<sup>34</sup> It appears that the graphite particles become less spherical with the addition of 1.8% *Al* into the ductile iron (Figure 5b,f) and after 3% *Al* addition, significant portion of graphite particles become exploded and had vermicular shape (Figure 5c,g). An example of an SEM image of extracted graphite by deep etching in *SiMo3Al* ductile iron is shown in Figure 5d.

The analysis of 3D sphericity of the graphite particles showed that 1.8% *Al* addition had a minimal effect, while 3% *Al* addition provided a shift to the left of the probability curve (Figure 6a), indicating an increased shape distortion. Also, *Al* alloying increased graphite particle Feret diameter in both ductile irons when compared to the base *SiMo* ductile iron (Figure 6b). This indicates that the *Al* segregation on graphite/austenite boundary affected the growth of graphite phase. In addition, some oxide bi-films were found in top part of the castings made from *Al*-alloyed ductile iron (Figure 6c); therefore, a top part of keel block was not used for specimens in this study.

Deep etching showed that precipitates at the eutectic grain boundary had a fan-shaped leaf (Figure 7a). EDX results indicate that the *Mo–Fe–C–Si* phases do not seem to

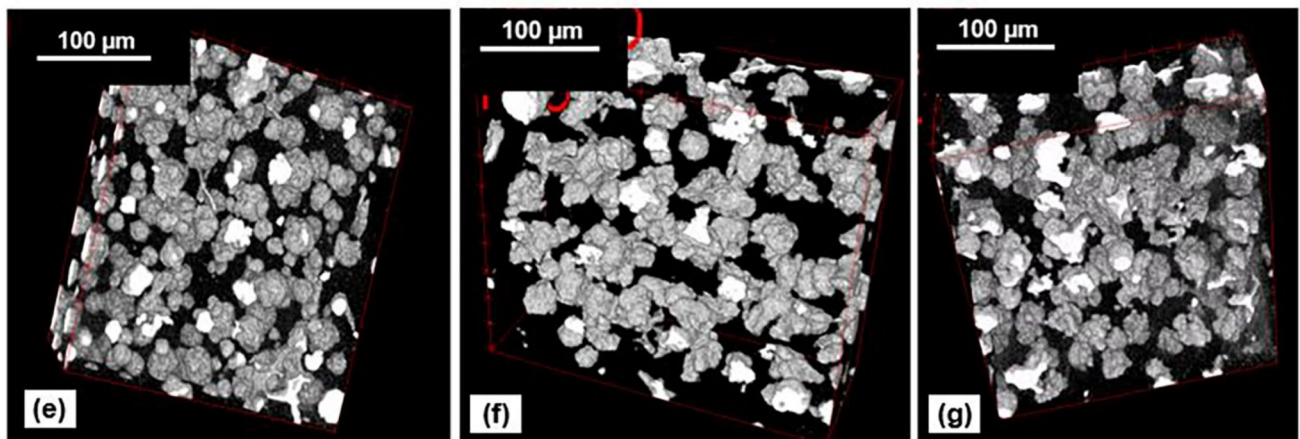
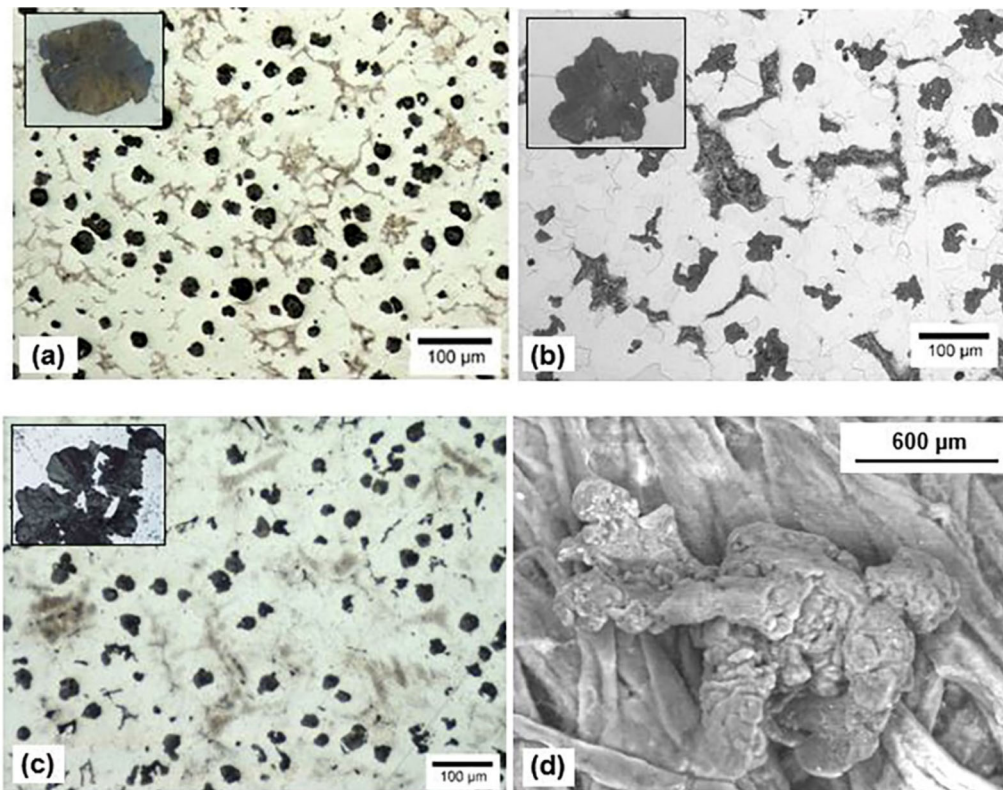


**Figure 5.** 2D optical microstructure and 3D  $\mu$ CT images of base SiMo (a, e), SiMo1.8Al (b, f), and SiMo3Al (c, g), and SEM image of extracted graphite particle from SiMo3Al ductile iron (d)

contain any Al (Figure 7b,c). Both Si and Al were present in the matrix ferrite in solid solution, and no visible specific precipitations, like  $\kappa$ -carbides, were found at applied SEM magnification.

**Dilatometry.** Thermal expansion was quantified using three sequential thermal cycles to define volume changes due to allotropic transformation, critical transformation temperatures, and dimensional stability. During the first thermal cycles (Figure 8), base SiMo ductile iron exhibited significant linear change at approximately 860 °C, as well as during cooling, which was related to allotropic transformation. Alloying by 1.8% Al and 3% Al significantly

reduced the linear change to 0.1% and to 0.03%, respectively. In addition, the Al alloying increased the critical temperatures during heating ( $A_c$ ) and cooling ( $A_r$ ) (Table 1). Aluminum alloying decreased the hysteresis of transformation temperature windows between heating and cooling cycles.

As shown in Figure 9, there were linear changes observed in the ductile irons when comparing the first and the third thermal cycles. The SiMo iron exhibited the largest indication of thermal instability during the thermal cycling as the continuous heating cycles significantly increased the absolute value of thermal expansion from first to third test.

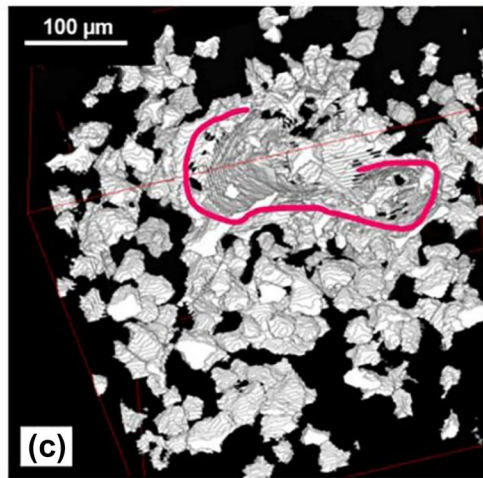
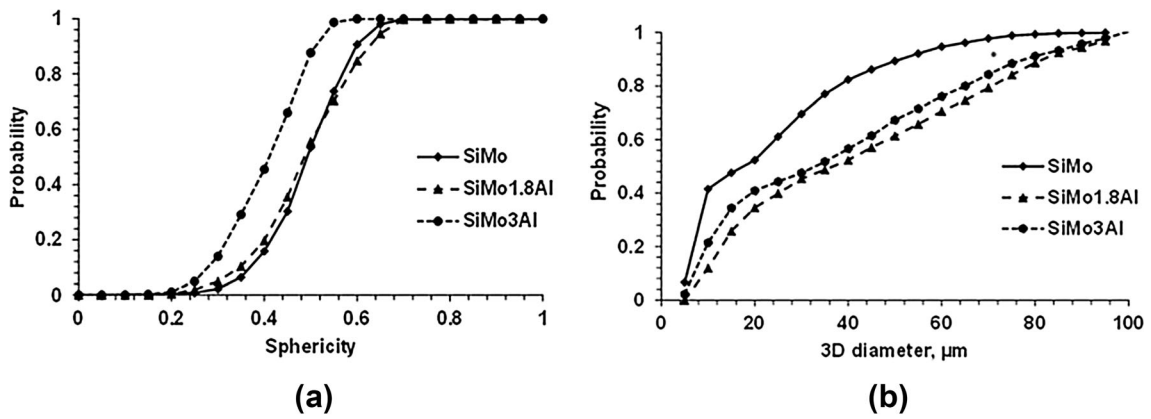


Figure 6. Statistic of 3D shape (a) and size (b) of graphite phase in alloys. Bi-film found in upper adjoint to riser SiMo3Al casting (c)

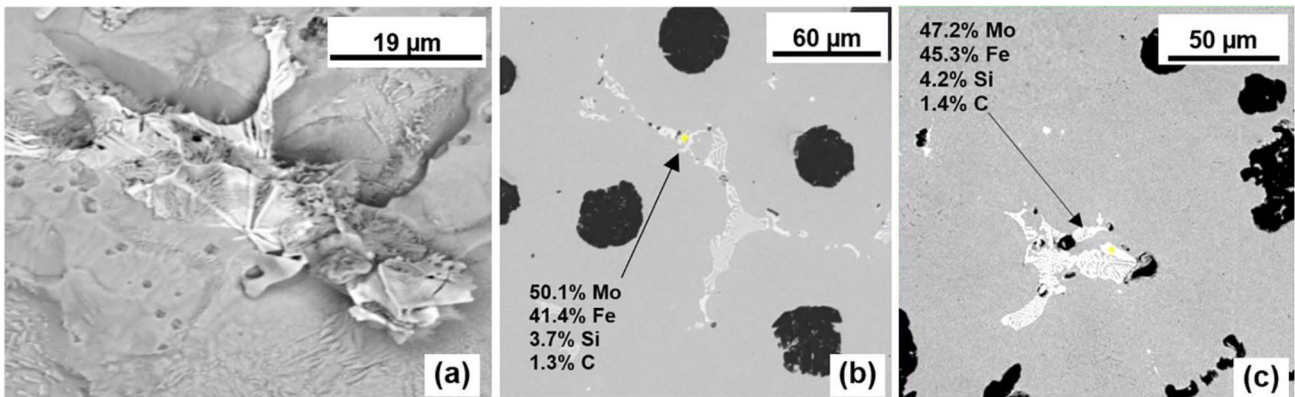


Figure 7. Interdendritic precipitates in deep etched base SiMo (a) and SEM/EDX analysis of carbides in base SiMo (b) and SiMo3Al (c) ductile irons

On the contrary, there were minimal changes in linear behavior between three thermal cycles for the SiMo3Al ductile iron as this alloy demonstrated stable expansion/contraction vs temperature dependencies. As shown in Figure 9b, the thermal stability of SiMo1.8Al was improved in comparison with the base but still was less as compared to the SiMo3Al ductile iron.

**Thermal Diffusivity.** It is well known that thermal cycling develops transient thermal conditions resulting in thermal gradients within a cast component, which can generate thermal stress. These stresses are influenced by both the coefficient of linear expansion and thermal diffusivity of a material. Figure 10 illustrates the measured thermal diffusivity between 200 °C and 900 °C for the base SiMo and SiMo3Al ductile irons tested by the laser flush method. In



both ductile irons, thermal diffusivity decreased significantly from 200 °C to 700 °C and increased above that temperature. The temperature of minimum thermal diffusivity was significantly below any eutectoid temperature and seems to be related to a Curie point. Alloying by Al decreased the thermal diffusivity at warm temperatures, maybe due to a ferrite alloying effect; however, this physical property was similar to the base material above 700 °C, possibly because of a positive effect of graphite nodule shape distortion on heat transfer.

*Static oxidation.* A methodology was used to decouple the major oxidation processes: oxidation of metallic components to form scale and decarburization (deC), which simultaneously occurred during high-temperature thermal exposure in SiMo ductile irons in air. These two processes result from different kinetics and influence each other; therefore, the total amount of reacted oxygen effecting oxidation and deC can vary with the test temperatures. In the base SiMo ductile iron, increasing test temperature above 750 °C dramatically intensified the deC; however, the oxidation rate of the scale formation was not as

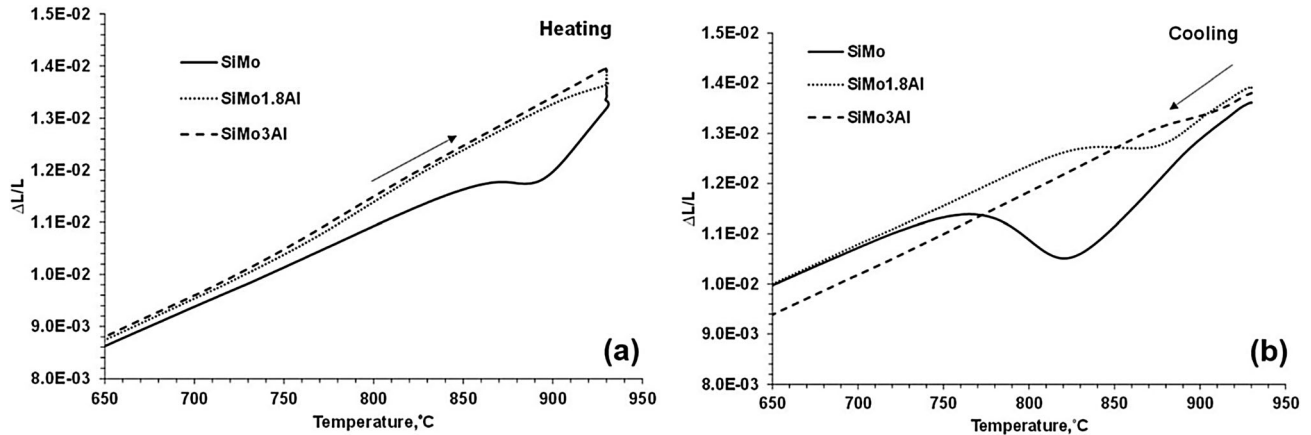


Figure 8. Expansion during heating (a) and contraction during cooling (b) of SiMo ductile irons (first cycle)

Table 1. Critical Temperatures (°C) Determined During Heating (Ac) and Cooling (Ar) at First Thermal Cycle

Alloy/method	Ac1	Ac3	Ar3	Ar1
SiMo (dilatometry)	855	890	825	765
(DSC)	860	920	—	—
SiMo1.8Al (dilatometry)	900	910	880	830
SiMo3Al (dilatometry)	—	—	900	880
(DSC)	895	945	—	—

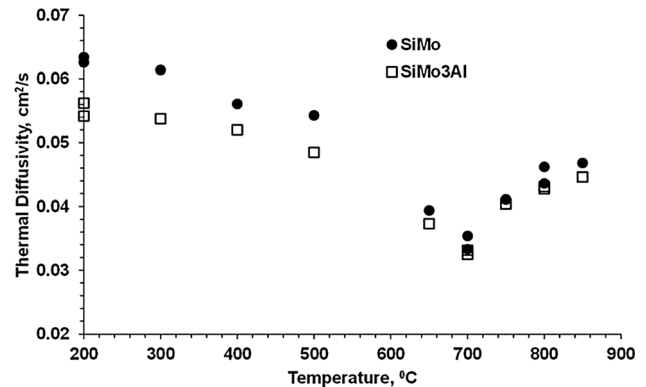


Figure 10. Thermal diffusivity of base and Al-alloyed SiMo ductile irons

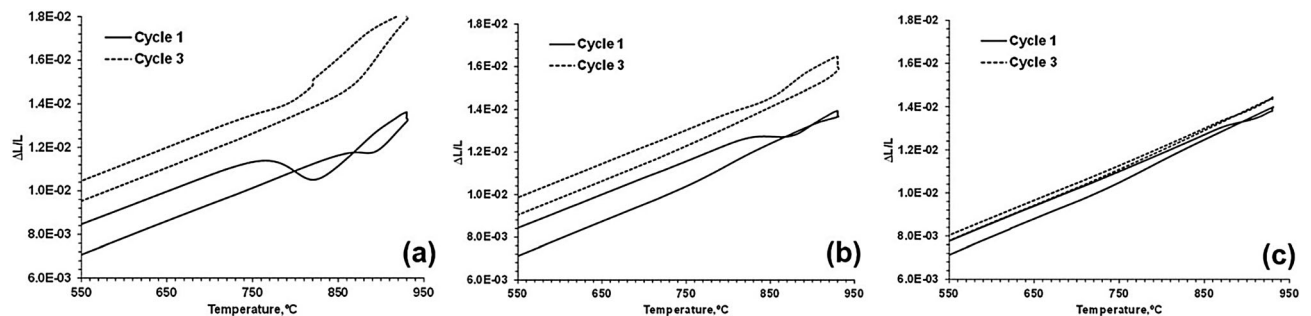
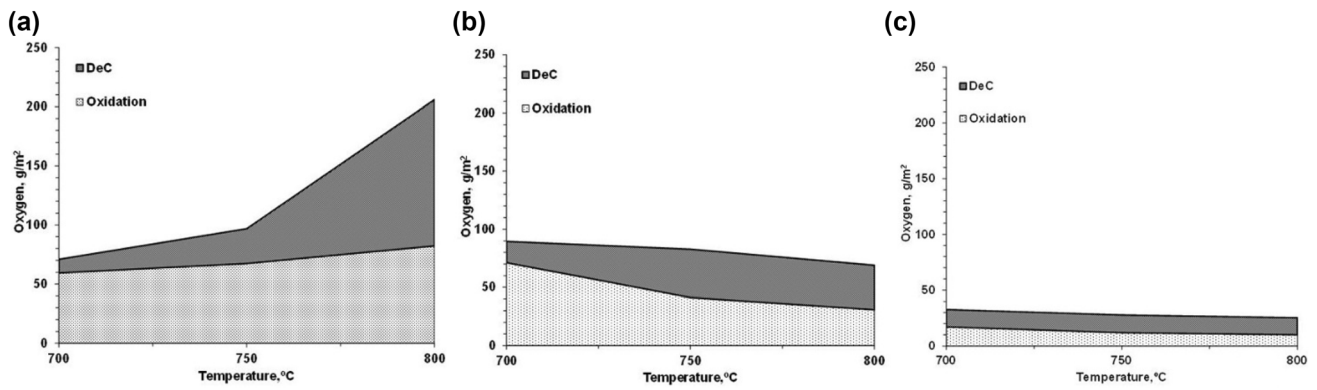


Figure 9. Dimensional stability of base SiMo (a) and alloyed by 1.8% Al (b) and 3% Al (c) ductile irons.



**Figure 11. Effect of temperature on oxidation and deC of SiMo (a), SiMo1.8Al (b), and SiMo3Al (c) ductile irons (air, 100 h)**

significant (Figure 11a). The static oxidation results in *SiMo3Al* ductile are much different: (i) the total amount of reacted oxygen for scale formation and deC was in order of magnitude less than in the base *SiMo* ductile iron and (ii) seemed oxidation rate slightly decreased with increasing test temperature (Figure 11c). The *SiMo1.8Al* ductile iron showed similar trends and minimum twice less oxidized and deC when compared to the base alloy (Figure 11b).

**Quasi-static mechanical properties.** High-temperature tensile tests at low strain rate indicated a softening effect when temperatures increased above 600 °C in all studied *SiMo* ductile irons. However, considering a minimum of a 75-MPa strength threshold, alloying by Al increased limiting working temperature by 60–75 °C, which is significant for high-temperature application (Figure 12).

**Thermocycling tests.** Thermocycling tests were performed using specimen geometry, which represented multiaxial thermomechanical load of constrained car manifold.<sup>31</sup> To verify the effect of oxidation on thermomechanical fatigue, thermocycling schedules included “short” (250 s cycle), “medium” (750 s cycle) and “long” (1350 s cycle) by

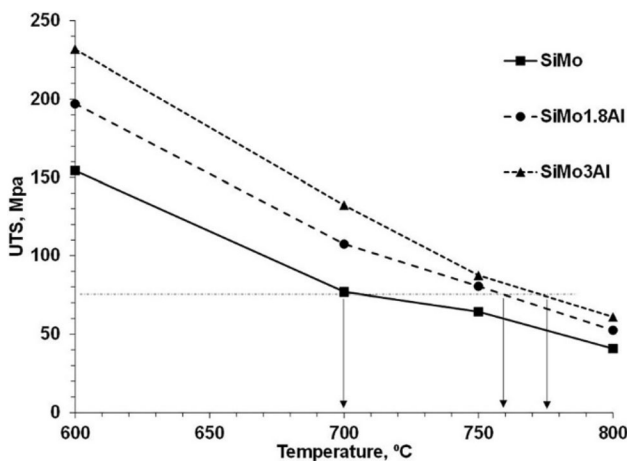


**Figure 12. Effect of temperature on tensile strength of SiMo, SiMo1.8Al, and SiMo3Al ductile irons**

varying holding times at upper temperature and applying the same temperature difference from 300 °C to 800 °C and heating/cooling rates. The relative value of maximum tensile stress at each cycle end was used as an indicator of crack initiation and propagation (Figure 13). A typical material response on test cycles is comprised of several periods: (i) initial strengthening (up to 100 cycles), (ii) followed by plastic softening (up to 200 cycles), (iii) overlapped with crack initiation which developed few small picks (100–300 cycles), and (iv) crack propagation with decreasing stress.

In the base *SiMo* ductile iron, increasing a high-temperature holding time from short to medium and long cycles drastically decrease the critical number of cycles for crack initiation (Figure 12a). During a short cycle, the base *SiMo* ductile iron developed a smooth curve, and the first cracks were observed after 300 cycles. However, when either the medium or long cycle was applied, the first peak of the force curve occurred in *SiMo* ductile iron before 100 cycles. This indicated a significant effect of intensive oxidation and deC on near-surface degradation. When testing the *SiMo1.8Al*, it demonstrated a different behavior as compared to the base *SiMo* ductile iron. When short cycles were used, the period of strengthening was shorter and the total number of cycles before critical crack development increased from 500 to 600 cycles. When testing the *SiMo3Al* ductile iron for a long-cycle schedule, the number of cycles for crack initiation increased more than 2 times as compared to the base *SiMo* ductile iron. In addition, the critical cycle number increased from 50 to 70%. The effect of oxidation on thermomechanical behavior of three alloys will be discussed in the next chapter.

### Analysis of Tested Ductile Irons and Discussion

Controlling high-temperature thermomechanical behavior of *SiMo* ductile iron by balancing the level of Al macro-alloying was investigated for different working conditions.

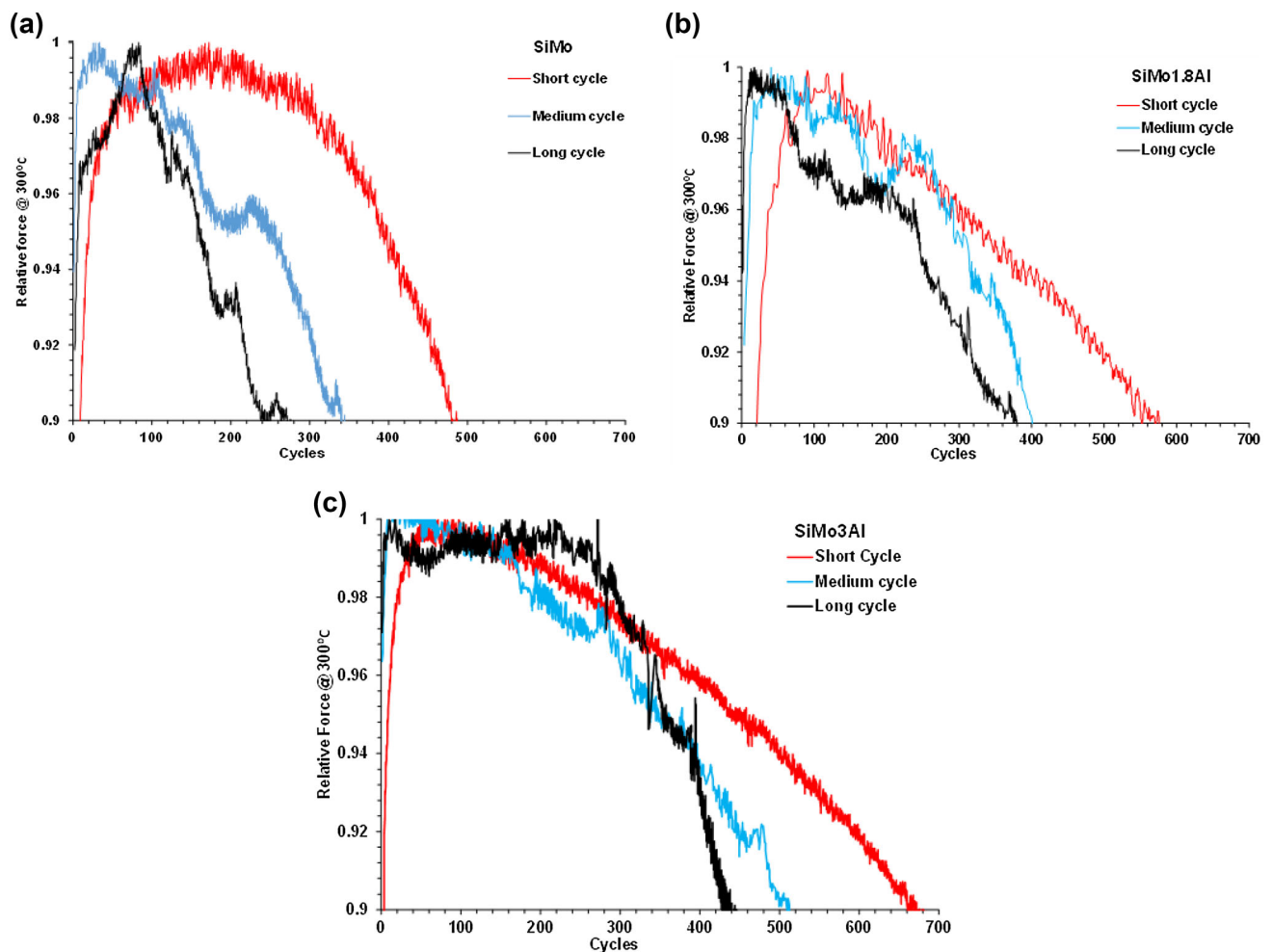


**Figure 13. Thermal cycling test results applying short, medium and long test schedules for industrial and laboratory SiMo (a), SiMo1.8Al (b) and SiMo3Al (c) ductile irons**

In the fully constrained thermomechanical test condition, thermal stress was due to the thermal expansion and contraction during thermal cycling. The intrinsic factors were related to physical (thermal diffusivity and linear expansion), mechanical (strength and plasticity at different temperatures), and chemical properties resulting in oxidation and deC. It was shown that levels of Al macro-alloying significantly influenced these physical, mechanical, and chemical properties. The high-temperature static and transient thermomechanical behavior in an oxidized environment could potentially be controlled by altering the alloying level. SEM/EDX,  $\mu$ CT and high-resolution TEM analyses were performed to better understand the mechanisms behind these differences.

When evaluating the baseline SiMo ductile iron, there were two types of surface degradation (oxidation and deC), which occurred simultaneously. As the temperature increased from 700 °C to 800 °C, the depth of deC layer dramatically increased (illustrated in top row SEM images in Figure 14 and quantified in Figure 11a). Non-destructive  $\mu$ CT analysis revealed irregularity of scale layer topology

(Figure 15a), which could be related to local crack formation (Figure 14) providing free passes for oxidant. The static oxidation rate drastically decreased in SiMo1.8Al and SiMo3Al alloys (Figure 11) by creating an additional alumina protection film at the matrix/scale interface (Figure 14 middle and bottom rows and Table 2). The experimentally observed multi-layered scale structure generally matched to the predicted by the thermodynamic simulations; however, resolution of applied SEM/EDX was not enough to clearly detect chemistry of submicron interface layer (Figure 3). The protection film in Al-alloyed ductile irons suppresses both metal and oxygen atomic diffusion. Temperature dependency of the oxygen allocated for scale formation indicates that increasing the test temperature improved protection efficiency of formed alumina film. The alumina film also dramatically decreased C and O diffusion, which suppressed the deC within the matrix material. However, non-spherical graphite particles in high Al-alloyed SiMo ductile iron (Figure 5) enabled a direct path for internal oxide growth, but internal oxidation was partially suppressed by forming an alumina protection film at graphite/matrix boundary. The  $\mu$ CT analysis of the oxide

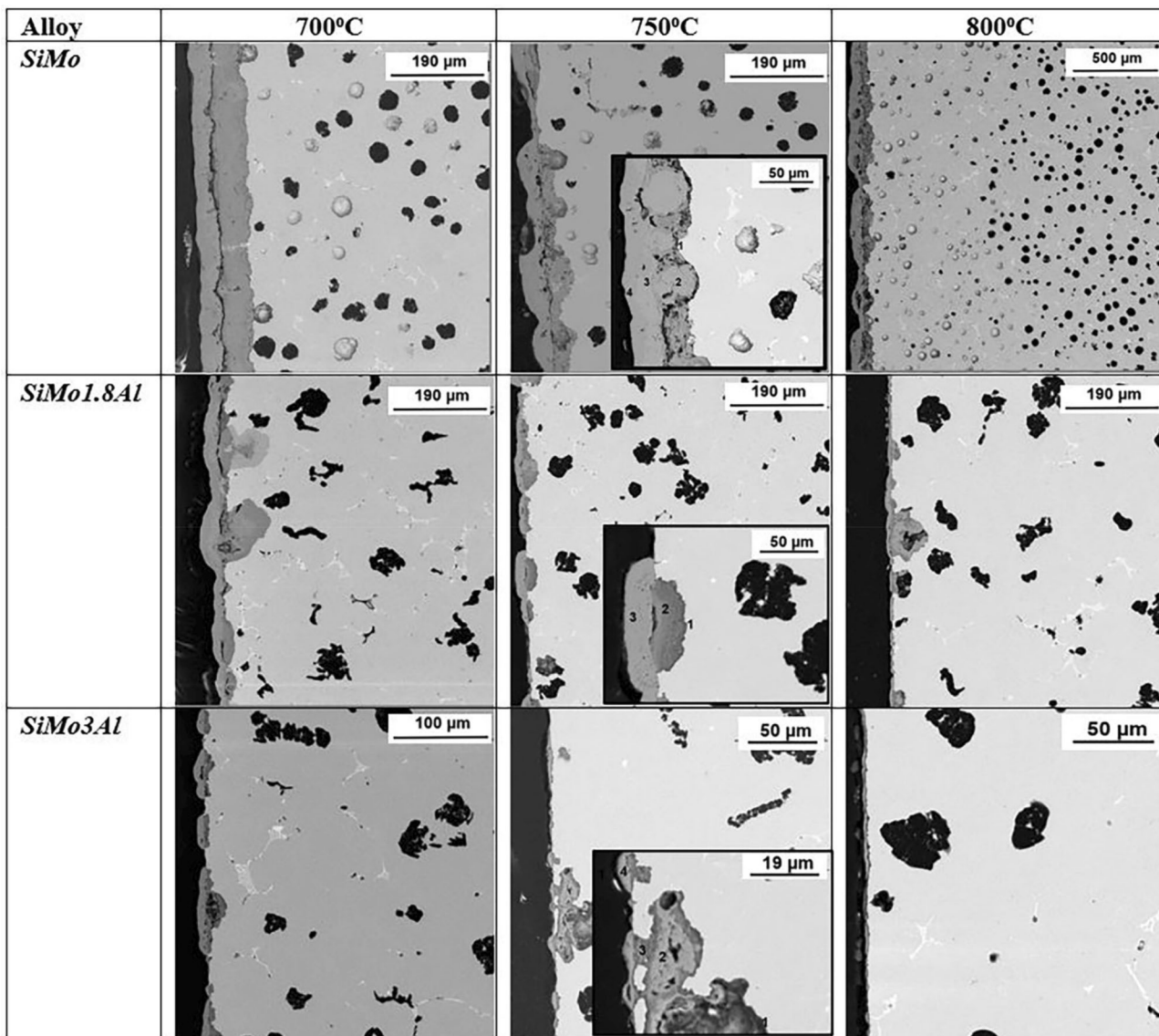


Figure 14. SEM/EDX images of oxidized in air alloy surfaces at 100 h

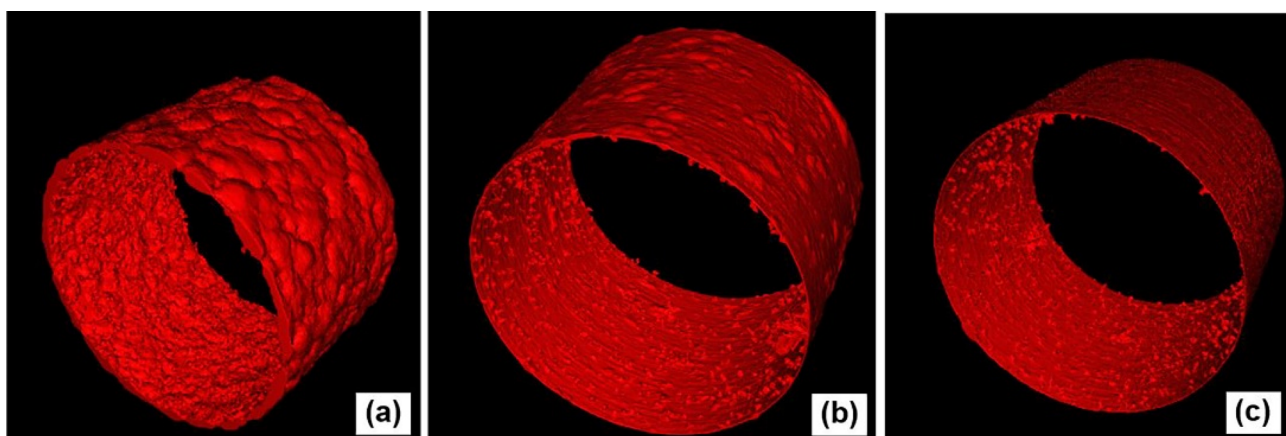


Figure 15. 3D rendered oxide layers in SiMo (a), SiMo1.8Al (b), and SiMo3Al (c) ductile irons oxidized in air at 800 °C during 100 h. Images were obtained from  $\mu$ CT scanning of 3-mm-diameter specimens.

**Table 2. EDX analysis (wt. %) of phases in oxidized surfaces (points from Figure 14)**

Alloy	Point layer	O	Fe	Si	Mn	Mo	Al	Ni
SiMo	1-interface	62	24	11	0.6	0.7	–	–
	2-internal	55	40	2.6	0.7	–	–	–
	3-external	51	47	–	0.6	–	–	–
	4-external	55	44	–	0.5	–	–	–
SiMo1.8Al	1-interface	50	32	3.4	0.5	–	9.6	3.2
	2-internal	58	31	3.8	0.5	–	3.7	2.0
	3-external	57	42	–	0.7	–	–	–
SiMo3Al	1-interface	53	36	2.1	0.6	–	6.2	0.6
	2-internal	60	38	0.4	0.4	–	0.8	–
	3-internal	59	29	2.3	0.4	–	6.7	1.1
	4-external	62	37	–	0.3	–	0.3	–

layers in Al-alloyed SiMo ductile irons is shown in Figure 15b,c and indicated some penetrations of the oxide into internal matrix, while the average thickness of external scale was significantly reduced as compared to the base alloy (Figure 15a).

Dilatometry tests of the SiMo ductile irons showed potential of the dimensional instability during thermal cycling (Figure 8). These tests were performed at nitrogen flow but did not exclude some amount of oxygen, so the dimensional instability could be related to near-surface reactions as well as internal changes in the matrix. The observed growth of the base SiMo ductile iron during the three thermal cycles mainly was related to deC reaction producing CO gas, which could plastically deform surface at the test temperature above 750 °C. The Al additions to the base alloy showed significantly better dimensional stability mainly by suppressing deC. Figure 16 illustrates the precipitation of complex Al-Fe-C and Mo carbide carbides formed at grain boundary during static oxidation test (100-

h holding at 800 °C). Fine submicron precipitations were also observed in statically oxidized SiMo3Al ductile iron. The revealed precipitates could κ-carbide, which is typically observed in heat-treated FeMnAlC steels.<sup>36</sup>

The outcomes of Al alloying of SiMo ductile iron depend on the thermal conditions, which could vary from static and quasi-static to highly transient. There was a clear indication of improved static oxidation resistance when Al was added to the alloy for both 1.8% and 3% concentrations. However, the effect of Al alloying on crack formation during thermocycling is more complicated as compared to static oxidation. In addition to oxidation resistance, there are other physical (linear expansion and thermal diffusivity) and mechanical (strength, plasticity, fatigue, creep) properties of material that are not linearly dependent on Al alloying. The addition of Al to the base alloy alters the microstructure of SiMo ductile iron in multiple ways, which include changes in Si and Al segregation, hardening of the bcc-Fe (ferrite) solid solution, facilitation of grain boundary precipitates, and degeneration of graphite shape. This study evaluated testing in near-quasi-static high-temperature oxidation conditions applying only few thermal cycles and transient thermal cycling. To characterize the three alloys discussed in this study, short, medium and long thermocycling schedules were applied for a fully constricted specimen (Figure 13). In all cases, increasing holding time at high temperature shortened the number of cycles for crack initiation (Figure 17a), which was defined visually during tests and quantified from the analysis of cycling curves. The critical crack propagation was compared to 90% threshold for maximal tensile forces generated during test cycles (Figure 17b). The test results showed that Al alloying could suppress crack initiation differently depending on oxidation period at each cycle. Virtual extension of the fitted lines to zero holding time in Figure 17a did not predict positive effect of Al alloying on crack initiation without oxidation, but number of cycles before crack initiation increased several times relative to the base SiMo ductile iron at longer cycling time. Effect of

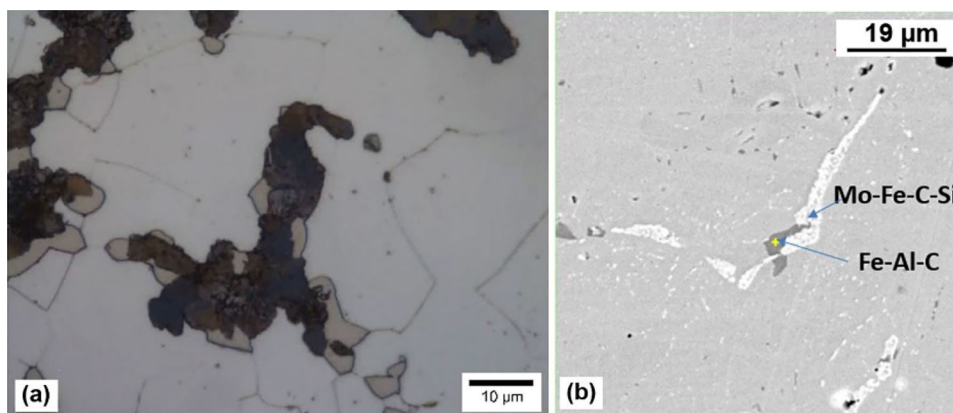


**Figure 16. Optical (a) and SEM images (b) of Fe-Al-C precipitates in the metal matrix of SiMo3Al ductile iron oxidized at 800 °C during 100 h**

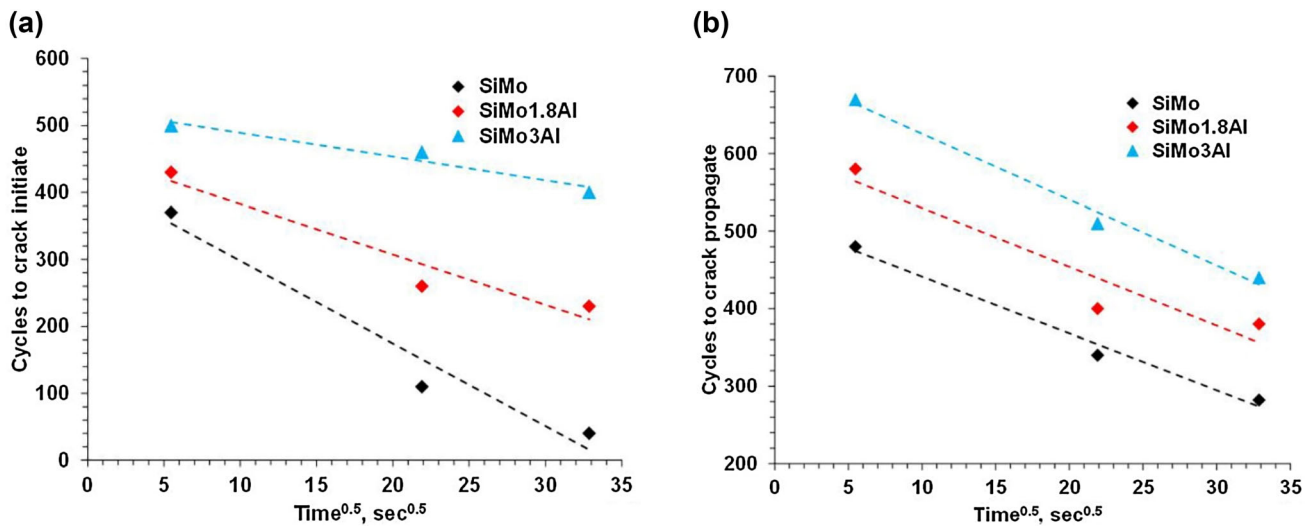


Figure 17. Effect of holding time during thermal cycles on number of cycles for crack initiation (a) and propagation (b) in base and Al-alloyed SiMo ductile irons

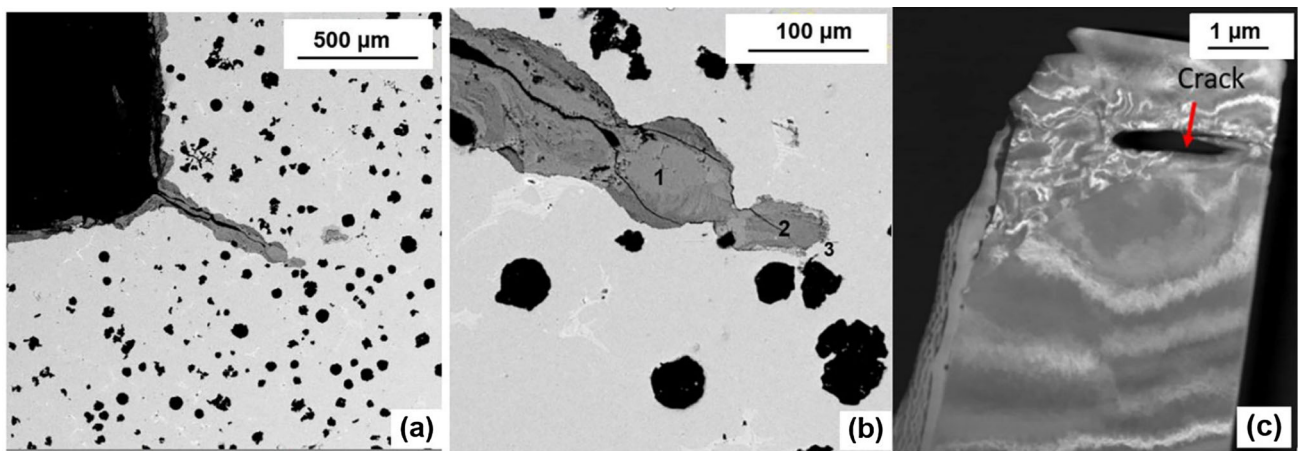


Figure 18. SEM images of thermal fatigue cracks formed in base SiMo ductile irons (short cycle) at low magnification (a) and higher magnification with EDX points (b), and TEM image of transfer section of crack tip (c)

Al alloying on crack propagation during thermal cycling was steady positive and less depended on oxidation time during each cycle (Figure 17b). In the recently published work,<sup>37</sup> the TMF life of *SiMo2.5Al* was longer by one or two orders of magnitude than *SiMo* iron, when at short high-temperature oxidation time was applied.

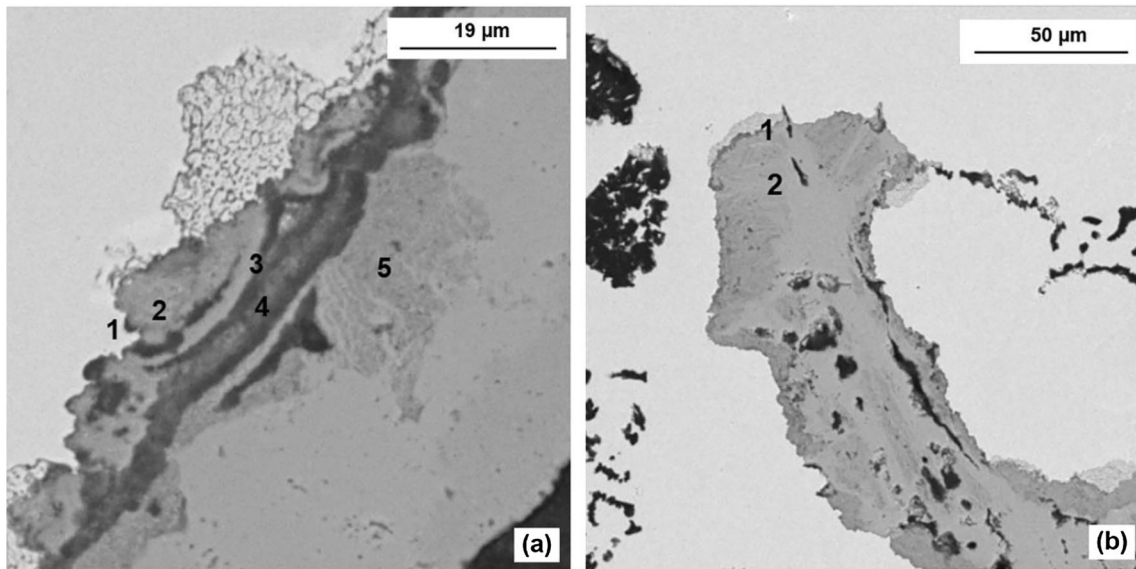
SEM analysis indicated that in the baseline *SiMo* ductile iron the crack propagation mainly takes place through the ferrite grain boundary from one to the other graphite nodules (Figure 18a,b, Table 3). High-resolution TEM image of transfer section perpendicular to crack direction, just near crack tip of 1 μm size, indicated that there was no actual silica oxide near the tip during short thermal cycling schedule. Thus, it is indicated that in this case, crack propagated mainly by mechanical fatigue and oxidation followed. Moreover, the formed oxide layer does not seem

Table 3. EDX analysis of phases in thermal cracks (points from Figure 18)

Alloy/cycle	Point	O	Fe	Si	Mn
<i>SiMo</i> /fast	1	58	41	–	1
	2	55	40	4	1
	3	51	42	9	–

to be enough to protect crack propagation during the next cycle.

The addition of 1.8% Al to the baseline alloy delayed the crack propagation during thermocycling when testing under short cycles and suppressed the crack initiation at thermal cycling with long holding time at high



**Figure 19. SEM images of thermal fatigue cracks formed in 1.8AlSiMo (a) and 3AlSiMo ductile irons (short cycle) (b)**

**Table 4. EDX analysis (wt. %) of phases in thermal cracks (points from Figure 19)**

Alloy/cycle	Point	O	Fe	Si	Mn	Al	Ni
SiMo1.8AlI	1	39	45	3	–	9	1
	2	51	43	3	1	1	–
	3	56	22	7	–	6	–
	4	65	24	7	–	5	–
	5	57	37	3	–	2	1
SiMo3AlI	1	50	39	3	1	6	–
	2	57	35	3	–	3	–

temperature. SEM analysis showed (Figure 19) that crack was only partially clogged by oxides during the short cycling, and it was completely filled by dense oxides during long thermal cycling. Scale chemistry had a mixture of *Fe–Si–Al* oxides (Table 4). A detailed high-resolution TEM analysis is shown in Figure 19. Foil was taken next to tip crack using FIB (red line in Figure 20a). During short cycle exposure, the surface of the tip of the crack was partially coated with a mixture of complex oxides, while a central part of crack had a void. Chemistry of phases, which were presented in different zones around crack (Figure 20b), is shown in Table 5.

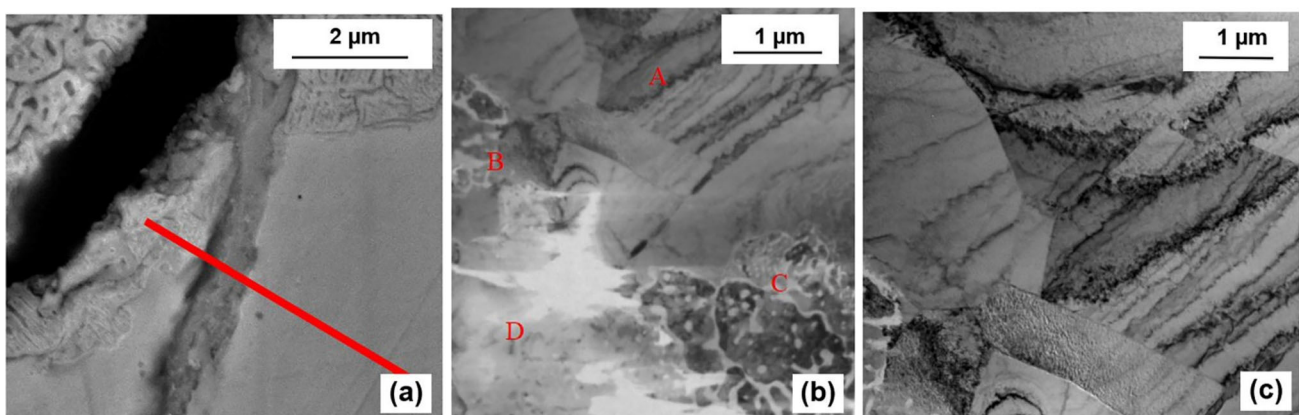


**Figure 20. Transverse section of crack tip in SiMo1.8Al ductile iron (short cycle): (a) SEM image with FIB extraction pass (red line) and TEM images of oxides next to crack surface (b) and sub-grains and dislocations in ferrite at crack boundary (c)**

**Table 5. EDX analysis (wt. %) of phases in thermal crack (zones from Figure 20)**

Zone	O	Fe	Si	Al	Mg
A, matrix, far from crack	–	90	6.1	1.9	
A, matrix close to crack	–	100	–	–	
B, Al–Si oxide	40.7	39	9.6	10.5	
C, mixture of oxides:					
SiO <sub>2</sub> (amorphous)	69	–	27.5	2.8	
Fe–Si–O (fayalite)	17	78	5.1	–	
D, mixture of oxides:					
Si–Al–O	77	–	16.6	5.8	–
Fe–Si–Al–O	70	6.8	17.2	5.4	–
Fe–Si–Al–Mg	63	21	6	2.9	3.2
Fe–O	48	51	–	–	–

It can be concluded that high-alloyed SiMo3Al ductile iron developed a strong alumina protection film during static oxidation, which improved oxidation resistance (Figure 11c) as well as resistance to crack growth during slowly changed thermomechanical conditions. However, degeneration of graphite particle shape in the SiMo3Al alloy negatively affected plasticity at room and warm temperatures, and this alloy did not experience protection from crack formation during rapid thermal cycling. The medium-alloyed SiMo1.8Al ductile iron has advantages at transient thermal cycling condition when both thermal stress and oxidation play a role in thermal fatigue in oxidized atmosphere.

## Conclusions

The effects of Al alloying on static and transient thermal behavior of SiMo ductile iron were investigated by combining thermodynamic simulations and experimental methods. 3D methods were used for structure characterization. Aluminum alloying decreased true sphericity of graphite particles; however, applied metal treatment minimized this negative effect at medium-alloying level. It was shown that Al alloying increased the temperature and decreased the volume change during the eutectoid transformation. These thermophysical property changes are important for high-temperature alloy performance. In addition, formed alumina film on scale/metal matrix interface suppressed the decarburization and stabilized the alloy dimensions during thermal cycling. A novel not destructive 3D CT method was used for non-destructive test of oxide-scale topology after static oxidation.

The specific thermal fatigue test procedure was designed to replicate self-induced strain during thermal cycling of constrained specimen with introducing triaxiality. High-

resolution TEM observation of crack tips formed during thermal cycling indicated different fracturing mechanisms.

In the baseline SiMo ductile iron, crack propagation occurred directly through the metal matrix, while in Al-alloyed SiMo ductile iron formed alumina films wrapped around the sharp crack tips and improved alloy durability during transient thermal conditions. In static oxidizing and slow/medium thermal cycling, SiMo3Al ductile iron showed superior protection against surface degradation. At the same time, graphite shape degeneration limited the resistance to cracking during rapid thermal cycling in this alloy. For such highly transient thermomechanical conditions, a medium-alloyed SiMo1.8Al ductile iron has advantages as compared to the baseline SiMo ductile iron.

## Acknowledgement

This material is based upon work supported by the U.S. Department of Energy's Office of Energy Efficiency and Renewable Energy (EERE) under the Award Number DE-EE0008458. We appreciate support from the Peaslee Steel Research Manufacturing Center at Missouri University of Science and Technology. We thank Dr. Wei-Ting Chen for TEM work and Dr. T. Selly for ICT analysis.

## Declarations

**Conflict of interest** On behalf of all authors, the corresponding author states that there is no conflict of interest.

**Open Access** This article is licensed under a Creative Commons Attribution 4.0 International License, which permits use, sharing, adaptation, distribution and reproduction in any medium or format, as long as you give appropriate credit to the original author(s) and the source, provide a link to the Creative Commons licence, and indicate if changes were made. The images or other third party material in this article are included in the article's Creative Commons licence, unless indicated otherwise in a credit line to the material. If material is not included in the article's Creative Commons licence and your intended use is not permitted by statutory regulation or exceeds the permitted use, you will need to obtain permission directly from the copyright holder. To view a copy of this licence, visit <http://creativecommons.org/licenses/by/4.0/>.

## REFERENCES

1. M. Ekström, S. Jonsson, High-temperature mechanical- and fatigue properties of cast alloys intended for use in exhaust manifolds. *Mater. Sci. Eng., A* **616**, 78–87 (2014)
2. N. Scheidhauer, C. Dommaschk, G. Wolf, Oxidation resistant cast iron for high temperature application. *Mater. Sci. Forum* **925**, 393–399 (2018)
3. M. Bartošák et al., Life assessment of SiMo 406 cast iron under LCF and TMF loading conditions. *Mater. High Temperat.* **36**(4), 285–295 (2018)



4. Standard SAE J2582: Standard Specification for High-Silicon Molybdenum Ferritic Iron Castings, SAE, 2018.
5. SAE International: Automotive Ductile Iron Castings for High Temperature Applications, SAE International, 2004.
6. S.H. Park et al.: Development of a Heat Resistant Cast Iron Alloy for Engine Exhaust Manifolds, SAE Technical Paper Series, SAE International, Technical Paper 2005-01-1688 (2005).
7. K.I.M. Yoon-Jun, J.A.N.G. Ho, O.H. Yong-Jun, High-temperature low-cycle fatigue property of heat-resistant ductile-cast irons. *Metal. Mater. Trans. A* **40A**, 2009 (2009)
8. S. Lekakh et al., Improving high-temperature performance of high Si-alloyed ductile iron by altering additions. *Inter Metalcast* **15**, 874–888 (2021). <https://doi.org/10.1007/s40962-020-00524-0>
9. S. Lekakh et al., Prevention of high-temperature surface degradation in simo cast irons by Cr and Al alloying. *Met. Mater. Trans. B* **51B**, 2542–2554 (2020)
10. M. Ekström, P. Szakalos, S. Jonsson, Influence of Cr and Ni on high-temperature corrosion behavior of ferritic ductile cast iron in air and exhaust gases. *Oxid. Met.* **80**(5–6), 455–466 (2013)
11. A. Kiani et al., Oxidation behaviour of Al-alloyed ductile cast irons at elevated temperature. *Surf. Interface Anal.* **36**(8), 1011–1013 (2004)
12. P. Kerdbua et al., High temperature corrosion behaviour of aluminide-coated cast iron for an exhaust manifold application. *Coatings* **10**(705), 1–15 (2020)
13. A. Ebel et al., High-temperature oxidation of a high silicon SiMo spheroidal cast iron in air with in situ change in H<sub>2</sub>O content. *Mater. Sci. Forum* **925**, 353–360 (2018)
14. R. González et al., Effects of high silicon contents on graphite morphology and room temperature mechanical properties of as-cast ferritic ductile cast irons Part II—Mechanical properties. *Mater. Sci. Eng. A* **712**, 803–811 (2018)
15. M. Ibrahim et al., Microstructure, hot oxidation resistance and damping capacity of Al- alloyed cast iron. *Int. J. Cast Met. Res.* **30**(2), 61–6916 (2017)
16. M.P. Brady et al. (2014) Long-Term Oxidation of Candidate Cast Iron and Stainless Steel Exhaust System Alloys from 650-800°C in Air with Water Vapor Oxidation of Metals, v. 82: 359-381
17. M. Sołński et al., Investigations of ferritic nodular cast iron containing about 5–6% aluminum. *Arch. Foundry Eng.* **16**, 141–146 (2016)
18. A.R. Kiani-Rashid, D.V. Edmonds, Phase transformation study of aluminium-containing ductile cast irons by dilatometry. *Mater. Sci. Eng., A* **481–482**, 752–756 (2008)
19. K. Papis, S. Tunzini, and W. Menk: Cast iron alloys for exhaust applications, In: 10th International Symposium on the Science and Processing of Cast Iron, Mar del Plata, Argentina (2014), Paper 07.
20. D. Franzen, P. Weiß, B. Pustal, A. Bührig-Polaczek, Influence of aluminium on silicon microsegregation in solution strengthened ductile iron. *Mater. Sci. Technol.* **35**(6), 687–694 (2019)
21. S. Gebhardt, J. Nellessen, A. Bührig-Polaczek, C. Broeckmann, Influence of aluminum on fatigue strength of solution-strengthened nodular cast iron. *Metals* **11**, 311 (2021)
22. J. Yaker et al., Microstructures and strength of aluminum containing gray and nodular irons in the temperature range 1200–1800F (649–982C). *AFS Trans.* **84**, 305–320 (1976)
23. J. David Rathnaraj, Thermomechanical fatigue analysis of stainless steel exhaust manifolds: *Int. J. Engineering Sci. Tech.* **2**(2), 265 (2012)
24. G.M. Castro Güizaa, W. Hormazab, A.R. Galvis Ec, L.M. Méndez Morenod, Bending overload and thermal fatigue fractures in a cast exhaust manifold. *Eng. Failure Anal.* **82**, 138 (2017)
25. J. Andersson et al., Thermo-Calc & DICTRA, computational tools for materials science. *Calphad* **26**(2), 273–312 (2002)
26. C. Yeung et al., Effect of homogenization treatment on segregation of silicon in ferritic ductile irons: a color metallographic study. *Mater. Sci. Technol.* **15**(7), 733–737 (1999)
27. A. Alhussein et al., Influence of silicon and addition elements on the mechanical behavior of ferritic ductile cast iron. *Mater. Sci. Eng., A* **605**, 222–228 (2014)
28. S. Lekakh et al., Effect of Si segregation on low temperature toughness of ductile iron. *AFS Trans.* **120**, 319–326 (2012)
29. H. Muhammad Muhmond, H. Fredriksson, Graphite growth control analysis in high Al cast iron. *Int. J. Cast Metals Res.* **29**(5), 272–278 (2016)
30. P. Chen et al., Abnormal expansion due to pearlite-to-austenite transformation in high aluminium-added steels. *Mater. Sci. Technol.* **32**(16), 1678–1682 (2016)
31. C. Bale et al., FactSage thermochemical software and databases. *Calphad* **26**(2), 189–228 (2002)
32. K. Shinzato et al., A laser flash apparatus for thermal diffusivity and specific heat capacity measurements. *J. Therm. Anal. Calorim.* **64**, 413–422 (2001)
33. S. Lekakh, M. Buchely, R. O'Malley, L. Godlewski, Li. Mei, Thermo-cycling fatigue of SiMo ductile iron using a novel thermo-mechanical Test intern. *J Fatigue* **148**, 106218 (2021)
34. O. Adaba et al.: Three-Dimensional Study of Inclusion Morphology and Size Distribution In Mn-Si Killed Steel, In: AIST Proceedings (2018) 2591–2600.
35. S. Lekakh et al., Quantitative  $\mu$ -CT analysis of scale topology formed during oxidation of high SiMo cast iron. *Oxid Met* **94**, 251–264 (2020)
36. S. Lekakh et. Al. (2019) 3D Characterization of Structure and Micro-porosity in Two Cast Irons with

Spheroidal Graphite Materials Characterization, 158: 109991

37. J. Campbell, *Complete Casting Handbook*, 2nd edn. (Elsevier, Oxford, UK, 2015)
38. L. Bartlett et al., An atom probe study of kappa carbide precipitation and the effect of silicon addition. *Met. Mater. Trans. A* **45A**, 2014–2421 (2014)
39. Quan, G., Li, D., and Wu, X.: Thermo-Mechanical Fatigue (TMF) Life of Ductile SiMo Cast Iron with

Aluminum Addition, SAE Technical Paper 2021-01-0281, 2021, <https://doi.org/10.4271/2021-01-0281>.

**Publisher's Note** Springer Nature remains neutral with regard to jurisdictional claims in published maps and institutional affiliations.